

# Nanoscale

Accepted Manuscript



This is an *Accepted Manuscript*, which has been through the Royal Society of Chemistry peer review process and has been accepted for publication.

*Accepted Manuscripts* are published online shortly after acceptance, before technical editing, formatting and proof reading. Using this free service, authors can make their results available to the community, in citable form, before we publish the edited article. We will replace this *Accepted Manuscript* with the edited and formatted *Advance Article* as soon as it is available.

You can find more information about *Accepted Manuscripts* in the [Information for Authors](#).

Please note that technical editing may introduce minor changes to the text and/or graphics, which may alter content. The journal's standard [Terms & Conditions](#) and the [Ethical guidelines](#) still apply. In no event shall the Royal Society of Chemistry be held responsible for any errors or omissions in this *Accepted Manuscript* or any consequences arising from the use of any information it contains.

Cite this: DOI: 10.1039/c0xx00000x

www.rsc.org/xxxxxx

**ARTICLE TYPE**

# A Single Multifunctional Nanoplatfom Based on Upconversion Luminescence and Gold Nanorods

Yue Huang,<sup>a</sup> Federico Rosei<sup>a, b</sup> and Fiorenzo Vetrone<sup>\*a, b</sup>

Received (in XXX, XXX) Xth XXXXXXXXXX 20XX, Accepted Xth XXXXXXXXXX 20XX

DOI: 10.1039/b000000x

Lanthanide-doped upconverting nanoparticles (UCNPs), which convert near-infrared (NIR) light to higher energy light have been intensively studied for theranostic applications. Here, we developed a hybrid core/shell nanocomposite with multifunctional properties using a multistep strategy consisting of a gold nanorod (GNR) core with an upconverting NaYF<sub>4</sub>:Er<sup>3+</sup>, Yb<sup>3+</sup> shell (GNR@NaYF<sub>4</sub>:Er<sup>3+</sup>, Yb<sup>3+</sup>). To use a single excitation beam, the GNR plasmon was tuned to ~650 nm, which is resonant with the upconverted red Er<sup>3+</sup> emission emanating from the <sup>4</sup>F<sub>9/2</sub> excited state. Thus, under laser irradiation at 980 nm, the intensity ratio of the upconverted green emission (arising from the <sup>2</sup>H<sub>11/2</sub> and <sup>4</sup>S<sub>3/2</sub> excited states of Er<sup>3+</sup>) showed a remarkable thermal sensitivity, which was used to calculate the temperature change due to rapid heat conversion from the GNR core. The red upconversion emission of the GNR@NaYF<sub>4</sub>:Er<sup>3+</sup>, Yb<sup>3+</sup> core/shell nanocomposite decreased compared with the NaYF<sub>4</sub>:Er<sup>3+</sup>, Yb<sup>3+</sup> nanoshell structure (without a GNR core), which indicates that energy transfer from NaYF<sub>4</sub>:Er<sup>3+</sup>, Yb<sup>3+</sup> to the GNR takes place, subsequently causing a photothermal effect. The anticancer drug, doxorubicin, was loaded into the GNR@NaYF<sub>4</sub>:Er<sup>3+</sup>, Yb<sup>3+</sup> nanocomposites and the drug release profile was evaluated. In particular, the release of doxorubicin was significantly enhanced at lower pH and higher temperature caused by the photothermal effect. This multifunctional nanocomposite, which is suitable for local heating and controlled drug release, shows strong potential for use in cancer therapy.

## 1 Introduction

Over the past decade, upconverting nanoparticles (UCNPs) have been studied extensively as versatile optical nanoprobess for a broad range of potential biomedical applications, due to their interesting and distinct optical properties. In particular, they have the unique ability to convert near-infrared (NIR) light to higher energies spanning the ultraviolet (UV), visible and NIR regions<sup>1-5</sup> through multiphoton absorption. Upconversion is ideal for applications in biology for a variety of reasons. For example, the excitation light in the NIR allows for remarkable light penetration depths *in vivo* as well as significantly reduced background autofluorescence.<sup>6</sup> Moreover, the NIR excitation light induces little or no phototoxicity to biological specimens.<sup>4, 5</sup> Up to now, an assorted array of UCNPs with a gamut of different morphologies has been investigated for a wide range of biological applications.<sup>5</sup> Among them, hollow UCNPs have been extensively studied since their large voids allow them to store a larger quantity of a particular cargo (compared to conventional UCNPs), for example, therapeutic drug molecules, and the shell could offer convenient channels for molecular permeation and diffusion.<sup>7, 8</sup> However, more importantly, combining other functional materials, such as superparamagnetic,<sup>9, 10</sup> silver,<sup>11</sup> and/or gold nanoparticles<sup>12</sup> with the UCNPs nanoshell structures, paves the way for the development of multifunctional core/shell nanostructures, which have potentially interesting applications in bioimaging, diagnosis and therapy, also known as theranostics.<sup>13</sup>

One of the most interesting recent developments is the use of UCNPs as non-invasive, contactless, optical nanothermometers

for living cells.<sup>14-17</sup> The majority of UCNP nanothermometers are based on the temperature dependent luminescence of the two green emissions of the Er<sup>3+</sup> ion (<sup>2</sup>H<sub>11/2</sub>→<sup>4</sup>I<sub>15/2</sub> and <sup>4</sup>S<sub>3/2</sub>→<sup>4</sup>I<sub>15/2</sub>) where their luminescence intensity ratios (LIR) vary as a function of temperature. These types of nanothermometers open the door for diagnostic possibilities since one of the first signs of many diseases (inflammation, cardiac issues or cancer) is often the appearance of thermal singularities.<sup>18</sup> Another envisioned use of nanothermometers is in combination with local nanoheaters whose main role is to cause contained temperature increases so as to induce cell death.<sup>19</sup>

One such use of localized heating is in photothermal therapy (PTT), a prospective cancer treatment strategy in which malignant cells are destroyed by local optical heating.<sup>20-24</sup> To generate a temperature increase in diseased cells, the photon energy is converted into heat from the excitation light source, more conveniently a laser, through optical absorption (due to its high power, monochromaticity, and ease of positioning to the pathological site). Nanoparticles with high optical absorption coefficients and thermal dissipation rates are expected to lead to an increase in PTT efficiency.<sup>25</sup> Gold nanorods (GNRs) are particularly apt in this regard and are considered as excellent candidates for PTT.<sup>26-28</sup> This is due to their strong, tunable surface plasmon resonance (SPR) absorption between 650 and 950 nm, especially when the plasmon is located in the NIR, making it compatible for *in vivo* applications. Moreover, GNRs have a larger absorption cross-section per unit mass compared with other gold nanomaterials possessing different morphologies, thereby leading to higher heating efficiencies.<sup>29, 30</sup>

One of the drawbacks of PTT, however, is that along with the diseased cells, healthy cells could be damaged due to the potentially large temperature increase. Therefore, care must be taken so as to not expose the surrounding healthy cells to this localized heating. This can be accomplished by incorporating local nanothermometers at the heating site, to optically monitor the local temperature in real time. To accomplish this, the nanothermometer and nanoheater must be located in the same cellular space and hence, should be transported together in the same vehicle. Thus, thermal sensing with UCNPs could ideally be used for controlling the hyperthermia treatment, which would minimize collateral damage in healthy tissues surrounding the hyperthermia target.

Previous studies have investigated the nanoheater/nanothermometer combination using two independent nanoparticles, for example, GNRs (the nanoheaters) and either Nd<sup>3+</sup>-doped LaF<sub>3</sub> nanoparticles<sup>19</sup> or CdSe quantum dots<sup>31</sup> (the nanothermometers) for controlled photothermal experiments. In this scenario, the individual heating and sensing nanoparticles do not easily overlap in space thereby making the experiment rather complex. Also, single LaF<sub>3</sub> nanoparticles heavily doped with Nd<sup>3+</sup>, that acted as both the heater and thermometer, were previously used for such experiments<sup>32,33</sup>. In another study, Debasu *et al.* prepared Gd<sub>2</sub>O<sub>3</sub>:Er<sup>3+</sup>, Yb<sup>3+</sup> nanorods with gold nanoparticles electrostatically coupled to their surfaces for simultaneous heating and thermometry applications.

Our hybrid nanoplatform has a GNR at the core with a solid outer shell of upconverting NaYF<sub>4</sub>:Er<sup>3+</sup>, Yb<sup>3+</sup>. It has also been reported that GNRs could be used for cargo release applications as the heat created could enhance the release of the stored cargo.<sup>35-37</sup> However, the simple use of GNRs possesses some limitations, including: limited loading amount of cargo on the surface and aggregation of the GNRs, due to the unstable cetyltrimethylammonium bromide (CTAB) bilayer, during which GNRs lose their unique optical properties. Recently, several strategies have been proposed to tackle these problems, including coating with silica,<sup>36, 37</sup> amphiphilic block copolymers,<sup>38</sup> and phospholipids.<sup>39-41</sup>

Here, we have designed a novel hybrid nanocomposite that exploits the unique optical properties of both these materials and combines them onto a single, solid nanoscale platform that also possesses a third modality, the capability of therapeutic drug release. We synthesized a core/shell multifunctional nanocomposite based on a GNR core enveloped in a layer of NaYF<sub>4</sub>:Er<sup>3+</sup>, Yb<sup>3+</sup> upconverting nanomaterial, loaded with a model drug to evaluate its release efficiency. This nanocomposite is expected to be suitable for bioimaging, and could potentially also be used for applications where a thermal gradient is required. In particular, this nanoscale vehicle has a "built-in" optical thermometer to monitor the local temperature increase. Finally, the NaYF<sub>4</sub>:Er<sup>3+</sup>, Yb<sup>3+</sup> shell allows for the release of a therapeutic moiety, which is enhanced by the heat optically generated from the GNR core.

## 2 Experimental Section

### 2.1 Materials

The lanthanide chlorides LnCl<sub>3</sub> (99.99%) Ln = (Y, Yb, Er), hydrogen tetrachloroaurate (III) hydrate (HAuCl<sub>4</sub>•3H<sub>2</sub>O), silver

nitrate (AgNO<sub>3</sub>, > 99%), L-Ascorbic acid (C<sub>6</sub>H<sub>8</sub>O<sub>6</sub>, > 99%), doxorubicin hydrochloride (DOX) were purchased from Alfa Aesar. Cetyltrimethylammonium bromide (CTAB), sodium tetrafluoroborate (NaBF<sub>4</sub>), sodium salicylate (99%), polyethylenimine (PEI), urea [CO(NH<sub>2</sub>)<sub>2</sub>], sodium borohydride (NaBH<sub>4</sub>, 99.99%) were purchased from Sigma Aldrich. Ultrapure deionized water (Millipore system) was used throughout the experiments. All the starting chemicals in this work were used without further purification.

### 2.2 Synthesis of Gold Nanorods (GNRs)

The seed solution for GNRs was prepared as reported previously.<sup>42</sup> Briefly, a 5 mL solution of 0.5 mM HAuCl<sub>4</sub> was mixed with 5 mL solution of 0.2 M CTAB. Subsequently, 0.60 mL of ice-cold 0.010 M NaBH<sub>4</sub> was added under vigorous stirring, which resulted in a color change from yellow to brownish-yellow. The seed solution was kept at room temperature before use.

For the preparation of the growth solution, 0.36 g of CTAB together with 0.032 g of sodium salicylate was dissolved in 10 mL of deionized water and the solution was kept at 30 °C. Subsequently, 0.24 mL of 4 mM AgNO<sub>3</sub> was added and kept undisturbed for 15 min where 10 mL of 1 mM HAuCl<sub>4</sub> was then added. After 15 min of slow stirring, 40 μL of 0.064 M ascorbic acid was slowly added to the mixture. The final step was the addition of 32 μL of the seed solution to the growth solution causing a gradual color change of the solution. The temperature of the growth solution was kept constant at 30 °C during the entire procedure.

### 2.3 Synthesis of Silica Coated GNRs (GNR@SiO<sub>2</sub>)

The synthesized GNRs were washed by centrifugation to remove excess CTAB surfactant. The sample was then dispersed in 10 mL of deionized water. After that, 100 μL of 0.1 M NaOH was added. Following this step, three 30 μL injections of 20% TEOS in methanol were added under gentle stirring at 30 min intervals. The mixture was stirred at room temperature for 2 days.

### 2.4 Synthesis of Y(OH)CO<sub>3</sub>:Er<sup>3+</sup>, Yb<sup>3+</sup> and GNR@SiO<sub>2</sub>@Y(OH)CO<sub>3</sub>:Er<sup>3+</sup>, Yb<sup>3+</sup> Nanosphere

The monodisperse Y(OH)CO<sub>3</sub>:Er<sup>3+</sup>, Yb<sup>3+</sup> colloidal nanospheres were prepared *via* a urea-based homogenous precipitation process.<sup>43</sup> In total, 1 mmol of LnCl<sub>3</sub>(Y:Yb:Er = 78:20:2) and 2 g of urea were dissolved in 100 mL of deionized water. The above solution was homogenized under magnetic stirring for 10 min. Subsequently, the mixture was heated to 90°C for 2 h with vigorous stirring. Finally, the obtained Y(OH)CO<sub>3</sub>:Er<sup>3+</sup>, Yb<sup>3+</sup> nanospheres were collected and washed with deionized water and ethanol several times. The preparation of GNR@SiO<sub>2</sub>@Y(OH)CO<sub>3</sub>:Er<sup>3+</sup>, Yb<sup>3+</sup> was similar to the above procedure except for the addition of 0.05 g of GNR@SiO<sub>2</sub> (synthesized previously) to the starting lanthanide chloride/urea solution.

### 2.5 Synthesis of NaYF<sub>4</sub>:Er<sup>3+</sup>, Yb<sup>3+</sup> Hollow Nanoshells or Core/Shell GNR@NaYF<sub>4</sub>:Er<sup>3+</sup>, Yb<sup>3+</sup> Nanocomposites

The NaYF<sub>4</sub>:Er<sup>3+</sup>, Yb<sup>3+</sup> hollow nanoshells were synthesized using a modified technique reported.<sup>44</sup> The obtained Y(OH)CO<sub>3</sub>:Er<sup>3+</sup>, Yb<sup>3+</sup> nanospheres were dispersed in 20 mL of deionized water using an ultrasonic bath. Then, 0.25 g PEI was added into the

above solution followed by ultrasonication and stirring. After that, 1 mmol of  $\text{NaBF}_4$  was added into the above mixture with continuous stirring for 10 min and the obtained solution was transferred to a 25 mL Teflon autoclave (VWR) and kept at  $110^\circ\text{C}$  for 3.5 h. The resulting dispersions were separated by centrifugation, washed with water, and then dried at  $80^\circ\text{C}$  for 12 h. A similar procedure was performed to prepare core-shell GNR@ $\text{NaYF}_4$  nanocomposites by replacing  $\text{Y}(\text{OH})\text{CO}_3:\text{Er}^{3+}, \text{Yb}^{3+}$  samples with GNR@ $\text{SiO}_2@Y(\text{OH})\text{CO}_3:\text{Er}^{3+}, \text{Yb}^{3+}$ .

## 2.6 DOX Loading and Release Experiments

GNR@ $\text{NaYF}_4:\text{Er}^{3+}, \text{Yb}^{3+}$  samples were mixed with 2 mL of DOX aqueous solution ( $1 \text{ mg mL}^{-1}$ ). The mixture was stirred at room temperature for 24 h to reach an equilibrium state. Next, the DOX-loaded samples were centrifuged and washed with phosphate buffer solution (PBS), the supernatant was collected and measured using UV-Vis spectrophotometer (Varian 5000) at a wavelength of 480 nm to determine the amount of DOX loading. The release behavior experiments were performed at  $37^\circ\text{C}$ . DOX loaded GNR@ $\text{NaYF}_4:\text{Er}^{3+}, \text{Yb}^{3+}$  nanocomposites were immersed in 2 mL PBS solution ( $\text{pH} = 7.4, 5.0$ ) with gentle stirring. At selected time intervals, the samples were centrifuged and the supernatant solution was collected and measured *via* the UV-Vis spectrophotometer, while fresh PBS was added again for further drug release experiments.

## 2.7 Characterization

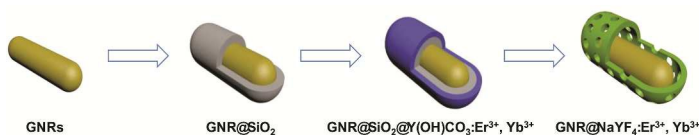
The crystal structures of all nanostructures under investigation were analyzed by X-ray spectroscopy (XRD, Bruker D8 Advanced Diffractometer, Cu  $K\alpha$  radiation). The UV-Vis spectra were examined using a UV-visible spectrometer (Varian 5000). The morphology and size distribution of various nanoparticles were observed from Transmission Electron Microscopy (TEM) images obtained with a Philips CM200 High-Resolution TEM (HRTEM). Luminescent measurements were carried out under 980 nm excitation light. The laser was focused on the sample using a lens to obtain a spot with a Gaussian intensity distribution with a 0.4 mm diameter. The emission light was collected by a lens in a 90 degrees configuration, and then transferred to a spectrophotometer (Avaspec - 2048L - USB2) using an optical fiber.

## 3 Results and Discussion

### 3.1 Synthesis and Characterization of GNR@ $\text{NaYF}_4:\text{Er}^{3+}, \text{Yb}^{3+}$

To prepare a multifunctional nanocomposite based on a GNR core and a  $\text{NaYF}_4:\text{Er}^{3+}, \text{Yb}^{3+}$  shell capable of inducing localized heating, thermal sensing, upconversion and drug release, a multistep synthetic method was employed and is summarized schematically in Scheme 1. Firstly, colloidal GNRs were prepared using aromatic additives, which reduced the amount of cytotoxic CTAB surfactant on the surface.<sup>45</sup> As shown in the TEM image, the length and width of GNRs were  $32.1 \pm 1.6$  and  $12.7 \pm 1.1 \text{ nm}$ , respectively, yielding an aspect ratio of approximately 2.5:1 (Figure 1A). With this aspect ratio, the GNRs had a longitudinal surface plasmon resonance (SPR) at 654 nm (*vide infra*). To mitigate the toxicity induced by the CTAB on their surface, the GNRs were then coated with a layer of silica

( $\text{SiO}_2$ ) and the thickness of the mesoporous silica shell reached roughly 12 nm (Figure 1B). As expected, the longitudinal SPR of the GNR@ $\text{SiO}_2$  nanorods shifts to longer wavelengths (Figure 2A) and after silica coating, the GNR@ $\text{SiO}_2$  have a longitudinal SPR peak located at 665 nm (a small red-shift of about 10 nm). This shift is ascribed to the larger refractive index of the silica layer (1.45) compared to water (1.33),<sup>46</sup> where the water, previously used as the medium surrounding the GNRs surface, was replaced by silica. Therefore, to induce a localized hot spot, optical irradiation at a wavelength of approximately 660 nm is required.



**Scheme 1** Schematic illustration of the synthetic procedure for the GNR@ $\text{NaYF}_4:\text{Er}^{3+}, \text{Yb}^{3+}$  nanocomposite.

Subsequently, to grow the final layer of  $\text{NaYF}_4:\text{Er}^{3+}, \text{Yb}^{3+}$ , the GNR@ $\text{SiO}_2$  surface was first coated with a stoichiometric lanthanide carbonate layer ( $\text{Y}(\text{OH})\text{CO}_3:\text{Er}^{3+}, \text{Yb}^{3+}$ ) using a urea-based homogenous precipitation process.<sup>43</sup> Figure 1C shows the prepared multilayer GNR@ $\text{SiO}_2@Y(\text{OH})\text{CO}_3:\text{Er}^{3+}, \text{Yb}^{3+}$  precursor structure. Finally, the outer  $\text{Y}(\text{OH})\text{CO}_3:\text{Er}^{3+}, \text{Yb}^{3+}$  precursor shell in the GNR@ $\text{SiO}_2@Y(\text{OH})\text{CO}_3:\text{Er}^{3+}, \text{Yb}^{3+}$  material was converted to  $\text{NaYF}_4:\text{Er}^{3+}, \text{Yb}^{3+}$  after hydrothermal treatment through the Kirkendall Effect.<sup>47-50</sup> Voids were formed during the transition of the outer layer from carbonate to fluoride and were attributed to the fact that the diffusion rate of the  $\text{Y}^{3+}$  ions inside to outside was more rapid than the diffusion rate of the  $\text{Na}^+$  and  $\text{F}^-$  ions from outside to inside. After a hydrothermal treatment at  $110^\circ\text{C}$  for 3.5 h, we observed that the morphology of the GNR@ $\text{NaYF}_4:\text{Er}^{3+}, \text{Yb}^{3+}$  nanocomposite material was maintained when compared with its GNR@ $\text{SiO}_2@Y(\text{OH})\text{CO}_3:\text{Er}^{3+}, \text{Yb}^{3+}$  precursor. The TEM images showed that the GNR@ $\text{NaYF}_4:\text{Er}^{3+}, \text{Yb}^{3+}$  nanocomposite material had sizes of *ca.* 150 nm, and the thickness of the  $\text{NaYF}_4:\text{Er}^{3+}, \text{Yb}^{3+}$  outer layer was approximately 24 nm (Figure 1D). Furthermore, the XRD patterns of the precursor GNR@ $\text{SiO}_2@Y(\text{OH})\text{CO}_3:\text{Er}^{3+}, \text{Yb}^{3+}$  nanoparticles confirm that the  $\text{Y}(\text{OH})\text{CO}_3:\text{Er}^{3+}, \text{Yb}^{3+}$  layer was amorphous and that following the hydrothermal treatment, it was transformed into hexagonal ( $\beta$ -) phase  $\text{NaYF}_4:\text{Er}^{3+}, \text{Yb}^{3+}$  (JCPDS file no. 28-1192) (Figure 2B). The XRD patterns of both the precursor and final materials showed peaks ascribed to the GNRs (JCPDS file no. 04-0784, marked with asterisks), which indicated the presence of GNRs in the nanostructure. On the basis of the TEM and XRD data, we can conclude that GNRs are in the core of the GNR@ $\text{NaYF}_4:\text{Er}^{3+}, \text{Yb}^{3+}$  nanocomposite, and that the initial precursor layer of  $\text{Y}(\text{OH})\text{CO}_3:\text{Er}^{3+}, \text{Yb}^{3+}$  was successfully transformed into hexagonal phase  $\text{NaYF}_4:\text{Er}^{3+}, \text{Yb}^{3+}$ . To further reveal the multilayered nanoarchitecture, compositional analysis by energy-dispersive X-ray microanalysis (EDX) indicated that Au, Na, Y, F elements were present in this nanocomposite (Figure 2C). Si was not observed, indicating that the  $\text{H}^+$  and  $\text{F}^-$  ions, which were

introduced in the  $\text{NaYF}_4:\text{Er}^{3+}, \text{Yb}^{3+}$  synthesis (*via* conversion of hydroxy carbonate to fluoride) would influence the leaching out of the silica. This allows for the creation of the hollow part of the nanoarchitecture.

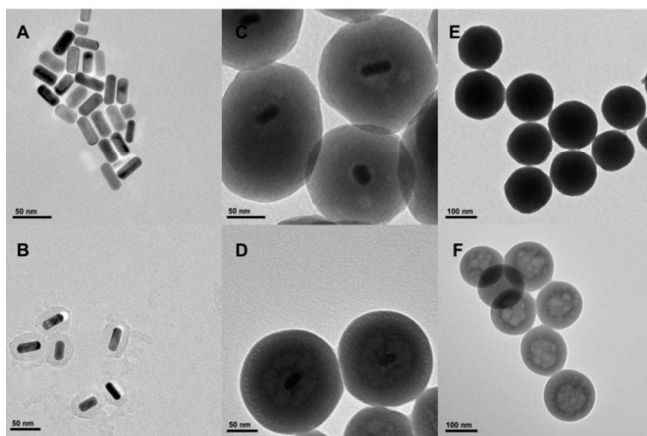


**Fig.1** TEM image of (A) synthesized GNRs, (B)  $\text{GNR@SiO}_2$ , (C)  $\text{GNR@SiO}_2@\text{Y(OH)CO}_3:\text{Er}^{3+}, \text{Yb}^{3+}$ , (D)  $\text{GNR@NaYF}_4:\text{Er}^{3+}, \text{Yb}^{3+}$ , (E)  $\text{Y(OH)CO}_3:\text{Er}^{3+}, \text{Yb}^{3+}$ , (F)  $\text{NaYF}_4:\text{Er}^{3+}, \text{Yb}^{3+}$  hollow nanoshells.

For comparative purposes, we also investigated hollow structured  $\text{NaYF}_4:\text{Er}^{3+}, \text{Yb}^{3+}$  nanoshells (without the GNR core). As we observed for the GNR based nanocomposite material discussed above, no obvious changes in size and morphology were detected in the TEM images of the  $\text{Y(OH)CO}_3:\text{Er}^{3+}, \text{Yb}^{3+}$  and  $\text{NaYF}_4:\text{Er}^{3+}, \text{Yb}^{3+}$  material, respectively. In addition, the TEM images demonstrate that the average sizes of both samples were approximately 147 nm, however, distinguishable circular voids and an outer nanometer sized shell were clearly visible for the  $\text{NaYF}_4:\text{Er}^{3+}, \text{Yb}^{3+}$  hollow nanoshells (Figure 1F). The crystallinity of the final  $\text{NaYF}_4:\text{Er}^{3+}, \text{Yb}^{3+}$  material was confirmed from the XRD (Figure 2B) and clearly showed that amorphous  $\text{Y(OH)CO}_3:\text{Er}^{3+}, \text{Yb}^{3+}$  was converted into pure hexagonal phase  $\text{NaYF}_4:\text{Er}^{3+}, \text{Yb}^{3+}$ .

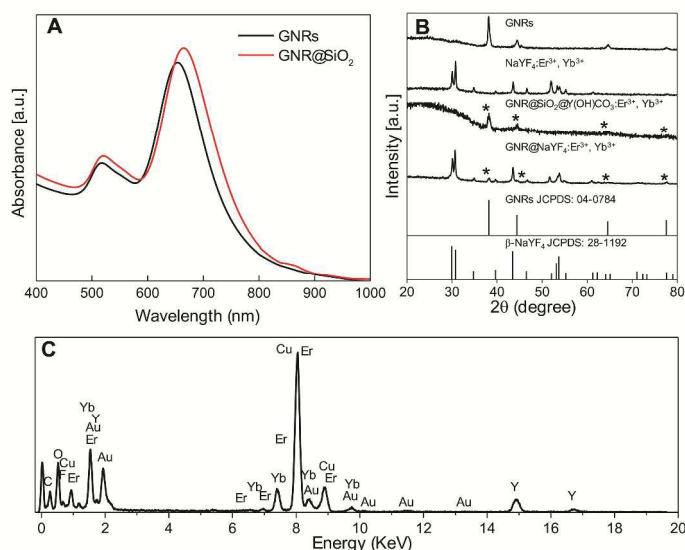


**Fig.2** (A) Extinction spectra of GNRs and  $\text{GNR@SiO}_2$ . (B) XRD pattern of (i) GNRs, (ii)  $\text{NaYF}_4:\text{Er}^{3+}, \text{Yb}^{3+}$ , (iii)  $\text{GNR@SiO}_2@\text{Y(OH)CO}_3:\text{Er}^{3+}, \text{Yb}^{3+}$ , (iv)  $\text{GNR@NaYF}_4:\text{Er}^{3+}, \text{Yb}^{3+}$ . The standard pattern of pure GNRs (JCPDS file No.

04-0784), pure hexagonal  $\text{NaYF}_4$  (JCPDS file No. 28-1192). The stars show the diffraction peaks of GNRs. (C) Elemental analysis of  $\text{GNR@NaYF}_4:\text{Er}^{3+}, \text{Yb}^{3+}$  by EDX

### 3.2 Upconversion Luminescence of $\text{NaYF}_4:\text{Er}^{3+}, \text{Yb}^{3+}$ and $\text{GNR@NaYF}_4:\text{Er}^{3+}, \text{Yb}^{3+}$

It is well known that  $\text{NaYF}_4:\text{Er}^{3+}, \text{Yb}^{3+}$  nanoparticles possess strong two-photon excited visible fluorescence (following absorption of two 980 nm photons) commonly referred to as upconversion.<sup>51</sup> This is due to co-doping with  $\text{Yb}^{3+}$  ions, which has a single excited state ( $^2\text{F}_{5/2}$ ) resonant with the pump wavelength (980 nm) as well as the first excited intermediate state of the luminescent  $\text{Er}^{3+}$  ion ( $^4\text{I}_{11/2}$ ) in the upconversion process. This results in efficient energy transfer from excited nearby  $\text{Yb}^{3+}$  ions bringing the  $\text{Er}^{3+}$  from its ground state ( $^4\text{I}_{15/2}$ ) to the first intermediate state ( $^4\text{I}_{11/2}$ ), which overlaps with the emission of the  $\text{Yb}^{3+}$  ion ( $^2\text{F}_{5/2} \rightarrow ^2\text{F}_{7/2}$ ). Concomitantly, a second excited  $\text{Yb}^{3+}$  ion in the same vicinity will also transfer its energy to the same  $\text{Er}^{3+}$  ion further exciting it to the  $^4\text{F}_{7/2}$  excited state.<sup>52,53</sup> Finally, green emission occurring from the  $^2\text{H}_{11/2}$  and  $^4\text{S}_{3/2}$  excited states to the  $^4\text{I}_{15/2}$  ground state as well as red emission from the  $^4\text{F}_{9/2}$  excited state to the  $^4\text{I}_{15/2}$  ground state is observed (see Figure 3D).

The upconverted emission intensities of the green  $^2\text{H}_{11/2} \rightarrow ^4\text{I}_{15/2}$  and  $^4\text{S}_{3/2} \rightarrow ^4\text{I}_{15/2}$   $\text{Er}^{3+}$  transitions have been shown to be sensitive to temperature.<sup>14</sup> This is because the two states are thermally coupled and follow a Boltzmann distribution

$$R = C \times \exp\left(\frac{-\Delta E}{kT}\right) \quad (1)$$

where  $R$  represents the luminescence intensity ratios (LIR) between the two green emissions of the  $\text{Er}^{3+}$  ion ( $^2\text{H}_{11/2} \rightarrow ^4\text{I}_{15/2}$  and  $^4\text{S}_{3/2} \rightarrow ^4\text{I}_{15/2}$ ),  $C$  is a constant,  $\Delta E$  is the energy gap between the two excited states,  $k$  is the Boltzmann constant and  $T$  is the temperature. In essence, the lower energy  $^4\text{S}_{3/2}$  state will thermally populate the higher  $^2\text{H}_{11/2}$  state since the two states are very close in energy (typically separated by only several hundred  $\text{cm}^{-1}$ ). As the temperature of the surroundings increase, the probability of the lower ( $^4\text{S}_{3/2}$ ) state thermally populating the higher ( $^2\text{H}_{11/2}$ ) state increases causing a change in the relative intensities of the two emission bands ( $^2\text{H}_{11/2} \rightarrow ^4\text{I}_{15/2}$  and  $^4\text{S}_{3/2} \rightarrow ^4\text{I}_{15/2}$ ). Thus, by exploiting the intensity ratio of these two emissions, it is possible to use  $\text{Er}^{3+}$ -doped materials as ratiometric thermal sensors. In fact, it was previously reported that  $\text{NaYF}_4:\text{Er}^{3+}, \text{Yb}^{3+}$  nanoparticles could be used as non-contact and non-invasive optical nanothermometers to measure the temperature of living HeLa cancer cells.<sup>14</sup> Here, our aim was to study the thermal behavior of the luminescence from the  $^2\text{H}_{11/2}, ^4\text{S}_{3/2} \rightarrow ^4\text{I}_{15/2}$   $\text{Er}^{3+}$  transitions in the hollow nanoshell  $\text{NaYF}_4:\text{Er}^{3+}, \text{Yb}^{3+}$  structure. Figure 3A presents two emission spectra of the  $\text{NaYF}_4:\text{Er}^{3+}, \text{Yb}^{3+}$  nanoshell at two different temperatures. As discussed above, we observed two emission bands centered at approximately 525 and 545 nm, owing to the  $\text{Er}^{3+}$  transitions from the  $^2\text{H}_{11/2}$  and  $^4\text{S}_{3/2}$  excited states to the  $^4\text{I}_{15/2}$  ground state (Figure 3D). It is unmistakable that the  $^2\text{H}_{11/2}:\text{S}_{3/2}$  luminescence intensity ratio (LIR) increases with temperature, and that this ratio increment also follows a linear relation with temperature, as can be observed in Figure 3B. Thus, experimental determination of how temperature governs this ratio can be used to create a calibration curve, which could in turn be used for luminescence-

based ratiometric thermal sensing.

After assessing the potential of the  $\text{NaYF}_4:\text{Er}^{3+}, \text{Yb}^{3+}$  nanoshell material to detect the local temperature, our goal here was to design a hybrid nanomaterial that was capable of both localized heating and possessing the simultaneous capacity to detect this temperature increment. Certain applications, for example PTT, do not require excessive heating and a temperature increment of only a few degrees could induce cell death. Rather than devise the hybrid material that possesses a GNR core with an SPR at the pump wavelength required for upconversion (980 nm) such that it could be directly excited with the laser beam, we opted for a different approach. This was done primarily since direct laser excitation of the GNR could induce a very large temperature gradient, which is not ideal for controlled PTT applications.<sup>54</sup> Thus, we chose to sensitize the GNR core indirectly using the upconverted red emission emanating from the  $\text{NaYF}_4:\text{Er}^{3+}, \text{Yb}^{3+}$  material. As previously shown, the GNR core has a longitudinal SPR centered at 660 nm, overlapping perfectly with the red emission from the  $\text{Er}^{3+} 4\text{F}_{9/2} \rightarrow 4\text{I}_{15/2}$  transition.

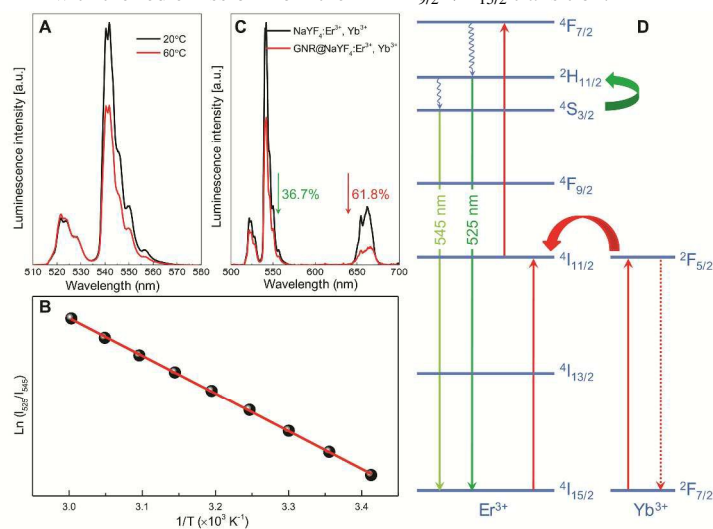


**Fig. 3** (A) Upconversion luminescence spectra of  $\text{NaYF}_4:\text{Er}^{3+}, \text{Yb}^{3+}$  at two different temperatures. (B) The temperature dependence of the ratio calculated from luminescence spectra. Dots are experimental results, and the red line is the best linear fit. (C) Upconversion luminescence spectra of  $\text{NaYF}_4:\text{Er}^{3+}, \text{Yb}^{3+}$  and  $\text{GNR@NaYF}_4:\text{Er}^{3+}, \text{Yb}^{3+}$ . (D) A scheme showing energy level of the  $\text{Yb}^{3+}$  and  $\text{Er}^{3+}$  dopant ions and upconversion mechanism. The temperature sensitivity of the  $\text{NaYF}_4:\text{Er}^{3+}, \text{Yb}^{3+}$  is the result of the closely spaced  $2\text{H}_{11/2}$  and  $4\text{S}_{3/2}$  energy states.

To further demonstrate the simultaneous heating and temperature sensing potential of the  $\text{GNR@NaYF}_4:\text{Er}^{3+}, \text{Yb}^{3+}$  hybrid nanocomposites, their upconversion emission was investigated at room temperature. From the detailed analysis of the data in Figure 3C, the upconverted  $2\text{H}_{11/2} : 4\text{S}_{3/2}$  emission ratio increased when compared with the emission of the  $\text{NaYF}_4:\text{Er}^{3+}, \text{Yb}^{3+}$  nanoshell structure at the same temperature. This change was due to the fact when exciting with the 980 nm wavelength, upconverted emission in the red region (from the  $4\text{F}_{9/2}$  excited state) is also obtained and is subsequently absorbed by the GNR at the center of this nanocomposite structure causing an appreciable temperature increment. To recap, the result of this temperature increment is the observed change in the relative

intensities of the upconverted green emissions (as previously described), which are sensitive to local temperature. The thermal change of  $\text{GNR@NaYF}_4:\text{Er}^{3+}, \text{Yb}^{3+}$  under NIR excitation was determined using the previously obtained calibration curve of the  $2\text{H}_{11/2} : 4\text{S}_{3/2}$  intensity ratios for the  $\text{NaYF}_4:\text{Er}^{3+}, \text{Yb}^{3+}$  nanoshell structure, and we calculated a temperature increase of 9 °C (the temperature of nanocomposites reached 34 °C) in the  $\text{GNR@NaYF}_4:\text{Er}^{3+}, \text{Yb}^{3+}$  nanocomposite. Again, this was attributed to the SPR absorption of the upconverted red light (660 nm) *via* energy transfer to the GNRs, which led to the rapid heat conversion. Meanwhile, it was observed from Figure 3C that the total emission intensity of  $\text{GNR@NaYF}_4:\text{Er}^{3+}, \text{Yb}^{3+}$  decreased (the decrease of green and red emissions were 36.7% and 61.8%, respectively) compared with the nanoshell  $\text{NaYF}_4:\text{Er}^{3+}, \text{Yb}^{3+}$  structure at the same temperature. It has been reported that the thickness of the spacer layer between a plasmonic metal nanostructure and fluorophore is a critical factor in determining whether the luminescence, in this case upconversion, is plasmonically enhanced or quenched.<sup>11, 12, 55</sup> Quenching could be caused when this spacer thickness is below a certain critical distance. For the synthesis of  $\text{GNR@NaYF}_4:\text{Er}^{3+}, \text{Yb}^{3+}$ ,  $\text{NaBF}_4$  was introduced to release  $\text{H}^+$  and  $\text{F}^-$  ions under high temperature and pressure,<sup>44</sup> causing the silica middle layer to simultaneously corrode. In this case, the red emission would be favorably absorbed by the GNR core and this quenching of the upconversion luminescence might be caused by non-radiative energy transfer from  $\text{NaYF}_4:\text{Er}^{3+}, \text{Yb}^{3+}$  to the gold surface. Figure 3C demonstrates that the red emission of the  $\text{GNR@NaYF}_4:\text{Er}^{3+}, \text{Yb}^{3+}$  decreases by 61.8%, which was significantly more than the decrease in green emission (36.7%). The position of the longitudinal SPR of the GNRs was determined to be ~660 nm from the UV-Vis absorption, which overlaps perfectly with the  $\text{NaYF}_4:\text{Er}^{3+}, \text{Yb}^{3+}$  red emission. Therefore, the red upconversion emissions will be preferentially absorbed compared to the green emissions, which accounts for both the observed photothermal effects as well as more prominent quenching compared to the green.

### 3.3 NIR Light-Triggered Drug Release

To examine the drug release behavior of this material, doxorubicin (DOX), an anticancer drug, was selected as a model drug to be loaded in the  $\text{GNR@NaYF}_4:\text{Er}^{3+}, \text{Yb}^{3+}$  nanocomposites. Thus, the loading level of the drug was investigated by the characteristic DOX optical absorbance at ~480 nm, and the loading efficiency was calculated to be 12.6 wt.% (Figure 4A). The cumulative DOX release profile from  $\text{GNR@NaYF}_4:\text{Er}^{3+}, \text{Yb}^{3+}$  was studied in two different PBS solutions at pH 7.4 and pH 5.0, respectively. As shown in Figure 4B, we observe an initial burst release of DOX within the first 2 h, followed by a sustained release over 12 h. This fast release in the first 2 h may be ascribed to the DOX molecules on the outer surface. Then, the diffusion of the DOX from the void to the outer upconverting  $\text{NaYF}_4:\text{Er}^{3+}, \text{Yb}^{3+}$  shell would proceed in a sustained manner. Meanwhile, the drug release profile shows a clear pH-dependent behavior, since the DOX release reached 20% after 48 h at pH 7.4. In contrast, when the pH value was adjusted to 5.0, 24% of the DOX was released with 2 h, and continuously increased to more than 45% after 48 h. This pH-induced controllable drug release trend would be beneficial for

localized cancer chemotherapy since the microenvironments of the extracellular tumor tissue and intracellular lysosomes and endosomes are acidic.<sup>56-58</sup> Thus, the GNR@NaYF<sub>4</sub>:Er<sup>3+</sup>, Yb<sup>3+</sup> nanocomposite could be considered as a promising material for future theranostic cancer studies.

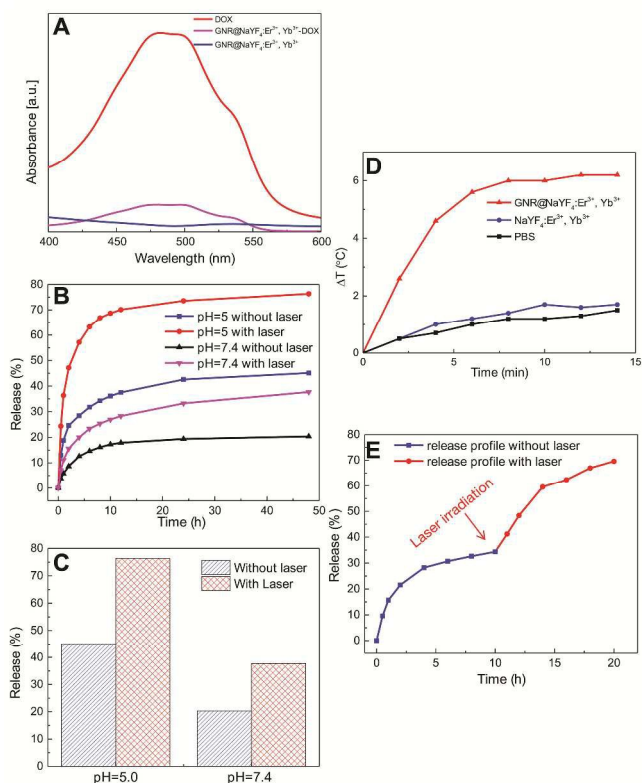


**Fig. 4** Drug loading and release behaviors. (A) Comparison of UV/Vis spectra of free DOX, GNR@NaYF<sub>4</sub>:Er<sup>3+</sup>, Yb<sup>3+</sup>-DOX, and GNR@NaYF<sub>4</sub>:Er<sup>3+</sup>, Yb<sup>3+</sup>. (B) DOX release profile of GNR@NaYF<sub>4</sub>:Er<sup>3+</sup>, Yb<sup>3+</sup> with and without laser irradiation at different pH value. (C) A comparison of DOX release content with and without laser irradiation at different pH value. (D) Temperature change of a 2.0 ml aqueous suspension of GNR@NaYF<sub>4</sub>:Er<sup>3+</sup>, Yb<sup>3+</sup> and control solution (NaYF<sub>4</sub>:Er<sup>3+</sup>, Yb<sup>3+</sup> and PBS) under laser irradiation. (E) DOX release profile of GNR@NaYF<sub>4</sub>:Er<sup>3+</sup>, Yb<sup>3+</sup> with and without laser irradiation.

In addition, DOX release was also studied under laser irradiation to assess whether the drug release is enhanced following plasmonic heating. With respect to the drug release at physiological pH (~7.4), it was observed to be much faster under 980 nm laser irradiation. We determined that the release rate was 18% higher than that without laser irradiation after 48 h (Figure 4C). Similar release behavior was observed when the pH value was adjusted to 5.0. At this pH, the DOX release rate reached 76% after 48 h under laser irradiation compared with 45% of DOX release without laser irradiation. As discussed previously, the SPR absorption around 660 nm of the core GNRs, coinciding with the red emission of NaYF<sub>4</sub>:Er<sup>3+</sup>, Yb<sup>3+</sup> under laser irradiation, results in a temperature increment, which in turn facilitates the release of the DOX molecules. To confirm that the heat generated was in fact due to the absorption of the red upconverted emission in the gold core and not from 980 nm laser heating, we carried out a controlled experiment. Under laser irradiation of the GNR@NaYF<sub>4</sub>:Er<sup>3+</sup>, Yb<sup>3+</sup> nanocomposites, we determined that the solution temperature in PBS increased by 6 °C after

approximately 7 min of irradiation and was stable for 15 min (measured with a thermocouple immersed in the PBS solution). This temperature increase was determined to be significantly more than the reference sample (hollow NaYF<sub>4</sub>:Er<sup>3+</sup>, Yb<sup>3+</sup> nanoshells and PBS) (Figure 4D). This confirmed that the temperature increase was in fact attributed to the efficient absorption of the NaYF<sub>4</sub>:Er<sup>3+</sup>, Yb<sup>3+</sup> red emission by the GNRs and not the absorption of the 980 nm laser by the water in the solution. In addition, another test of the drug release was investigated when the release process was carried out in PBS (pH = 5.0) for 10 h without laser irradiation, followed by continued laser irradiation for another 10 h. As shown in Figure 4E, we can clearly observe that 34% of the DOX was released without irradiation for first 10 h, while a greater release was demonstrated to be triggered by laser irradiation, which released DOX up to 69%. Again, this result confirms that laser irradiation could effectively control drug release by causing local heating from the GNRs to increase the diffusion of the DOX from the nanocomposite.

## 4 Conclusions

In summary, we developed a multifunctional nanoplatform composed of a GNR core and an outer shell of upconverting NaYF<sub>4</sub>:Er<sup>3+</sup>, Yb<sup>3+</sup>. This nanocomposite was capable of inducing a localized heating *via* the GNR core while the outer shell could be used to simultaneously monitor the surrounding temperature increases. Heating is generated by absorption of the upconverted red light from the Er<sup>3+</sup> <sup>4</sup>F<sub>9/2</sub> → <sup>4</sup>I<sub>15/2</sub> transition, which overlaps perfectly with the SPR of the gold core. The absorption from the GNR core was evidenced by the more drastic quenching of the red compared to the green transitions. The relative intensities of the upconverted emissions from the <sup>2</sup>H<sub>11/2</sub> → <sup>4</sup>I<sub>15/2</sub> and <sup>2</sup>S<sub>3/2</sub> → <sup>4</sup>I<sub>15/2</sub> transitions were sensitive to temperature and allowed the outer NaYF<sub>4</sub>:Er<sup>3+</sup>, Yb<sup>3+</sup> shell to act as a nanothermometer. Finally, when this nanocomposite was loaded with a model anti-cancer drug, we showed that this photothermal effect could trigger fast drug release, especially at low pH values. This drug release behavior, which depends on high temperature and low pH, is favorable in tumor extracellular environment, and hence has promising applications in cancer therapy.

## Acknowledgements

F.V. and F.R. acknowledge funding from the Natural Sciences and Engineering Research Council (NSERC Discovery Grants) of Canada and Fonds de recherche du Québec - Nature et technologies (FRQNT) for supporting this research. F.V. also wholeheartedly thanks the Fondation Sibylla Hesse for funding. Y.H. acknowledges financial support from the Merit Scholarship Program for Foreign Students from the Ministère de l'Éducation, du Loisir et du Sport du Québec. F.R. is grateful to the Canada Research Chairs program for partial salary support and acknowledges NSERC for an EWR Steacie Memorial Fellowship. F.R. is also grateful to the AvH Foundation for a FW Bessel Award.

## Notes and References

- <sup>a</sup> Institut National de la Recherche Scientifique - Énergie, Matériaux et Télécommunications, Université du Québec, 1650 Boulevard Lionel-Boulet, Varennes, Québec J3X 1S2, Canada.
- <sup>b</sup> Centre for Self-Assembled Chemical Structures, McGill University, 5 Montreal, QC, H3A 2K6 (Canada).  
Email:vetrone@emt.inrs.ca
- 1 F. Wang, D. Banerjee, Y. Liu, X. Chen, X. Liu. *Analyst*, 2010,**135**,1839-1854.
  - 2 J. Zhou, Z. Liu, F. Li. *Chem Soc Rev.*, 2012,**41**,1323-1349.
  - 3 D.K. Chatterjee, M.K. Gnanasamandhan, Y. Zhang. *Small*, 2010,**6**,2781-2795.
  - 4 M. Wang, G. Abbineni, A. Clevenger, C. Mao, S. Xu. *Nanomedicine*, 2011,**7**,710-729.
  - 5 J. Shen, L. Zhao, G. Han. *Adv Drug Deliv Rev.*, 2013,**65**,744-755.
  - 6 S. Nagarajan, Y. Zhang. *Nanotechnology*, 2011,**22**, 395101.
  - 7 W.R. Zhao, H.R. Chen, Y.S. Li, L. Li, M.D. Lang, J.L. Shi. *Adv. Func. Mater.*, 2008,**18**,2780-2788.
  - 8 Z.G. Feng, Y.S. Li, D.C. Niu, L. Li, W.R. Zhao, H.R. Chen, et al. *Chem. Commun.*, 2008, **23**, 2629-2631.
  - 9 F. Zhang, G.B. Braun, A. Pallaro, Y.C. Zhang, Y.F. Shi, D.X. Cui, et al. *Nano Lett.*, 2012,**12**,61-67.
  - 10 X.J. Zhu, J. Zhou, M. Chen, M. Shi, W. Feng, F.Y. Li. *Biomaterials*. 2012,**33**,4618-4627.
  - 11 F. Zhang, G.B. Braun, Y.F. Shi, Y.C. Zhang, X.H. Sun, N.O. Reich, et al. *J. Am. Chem. Soc.*, 2010,**132**,2850-2851.
  - 12 W. Ge, X.R. Zhang, M. Liu, Z.W. Lei, R.J. Knize, Y.L. Lu. *Theranostics*, 2013,**3**,282-288.
  - 13 X. Kang, C. Li, Z. Cheng, P. Ma, Z. Hou, J. Lin. *Wiley Interdiscip Rev Nanomed Nanobiotechnol*. 2014,**6**,80-101.
  - 14 F. Vetrone, R. Naccache, A. Zamarron, A.J. de la Fuente, F. Sanz-Rodríguez, L.M. Maestro, et al. *ACS Nano*, 2010,**4**,3254-3258.
  - 15 N.N. Dong, M. Pedroni, F. Piccinelli, G. Conti, A. Sbarbati, J.E. Ramirez-Hernandez, et al. *ACS Nano*, 2011,**5**,8665-8671.
  - 16 C.D.S. Brites, P.P. Lima, N.J.O. Silva, A. Millan, V.S. Amaral, F. Palacio, et al. *Nanoscale*, 2012,**4**,4799-4829.
  - 17 D. Jaque, F. Vetrone. *Nanoscale*, 2012,**4**,4301-4326.
  - 18 M. Stark. *Cancer*, 1974, **33**, 1664-1670.
  - 19 U. Rocha, C. Jacinto, W.F. Silva, I. Guedes, A. Benayas, L.M. Maestro, et al. *ACS Nano*, 2013,**7**,1188-1199.
  - 20 L.C. Kennedy, L.R. Bickford, N.A. Lewinski, A.J. Coughlin, Y. Hu, E.S. Day, et al. *Small*, 2011,**7**,169-183.
  - 21 X.H. Huang, I.H. El-Sayed, W. Qian, M.A. El-Sayed. *J. Am. Chem. Soc.*, 2006,**128**,2115-2120.
  - 22 X.H. Huang, P.K. Jain, I.H. El-Sayed, M.A. El-Sayed. *Laser. Med. Sci.*, 2008,**23**,217-228.
  - 23 P.K. Jain, X.H. Huang, I.H. El-Sayed, M.A. El-Sayed. *Acc. Chem. Res.*, 2008,**41**,1578-1586.
  - 24 J.L. Li, M. Gu. *IEEE J. Sel. Top. Quant.*, 2010,**16**,989-996.
  - 25 A.O. Govorov, H.H. Richardson. *Nano Today*, 2007,**2**,30-38.
  - 26 A.M. Alkilany, L.B. Thompson, S.P. Boulos, P.N. Sisco, C.J. Murphy. *Adv. Drug Delivery Rev.*, 2012,**64**,190-199.
  - 27 W.I. Choi, A. Sahu, Y.H. Kim, G. Tae. *Ann. Biomed. Eng.*, 2012,**40**,534-546.
  - 28 Z.J. Zhang, J. Wang, C.Y. Chen. *Theranostics*. 2013,**3**,223-238.
  - 29 S. Link, M.B. Mohamed, M.A. El-Sayed. *J. Phys. Chem. B*, 1999,**103**,3073-3077.
  - 30 L.M. Maestro, P. Haro-González, A. Sánchez-Iglesias, L.M. Liz-Marzán, J. G. Solé, D. Jaque. *Langmuir*, 2014,**30**,1650-1658.
  - 31 L.M. Maestro, P. Haro-González, M.C. Iglesias-de la Cruz, F. Sanz-Rodríguez, Á. Juarranz, J.G. Solé, D. Jaque. *Nanomedicine*, 2013,**8**,379-388.
  - 32 E. Carrasco, B. Rosal, F. Sanz-Rodríguez, Á. Juarranz, P.H. Gonzalez, U. Rocha, K.U. Kumar, C. Jacinto, J.G. Solé, D. Jaque. *Adv. Funct. Mater.*, 2015,**25**,615-626.
  - 33 U. Rocha, K.U. Kumar, C. Jacinto, J. Ramiro, A.J. Caamano, J.G. Solé, D. Jaque. *Appl. Phys. Lett.*, 2014,**104**,053703.
  - 34 M.L. Debasu, D. Ananias, I. Pastoriza-Santos, L.M. Liz-Marzán, J. Rocha, L.D. Carlos. *Adv. Mater.*, 2013,**25**,4868-4874.
  - 35 J. You, R.P. Shao, X. Wei, S. Gupta, C. Li. *Small*. 2010,**6**,1022-1031.
  - 36 Z.J. Zhang, L.M. Wang, J. Wang, X.M. Jiang, X.H. Li, Z.J. Hu, et al. *Adv. Mater.*, 2012,**24**,1418-1423.
  - 37 S. Shen, H.Y. Tang, X.T. Zhang, J.F. Ren, Z.Q. Pang, D.G. Wang, et al. *Biomaterials*, 2013,**34**,3150-3158.
  - 75 K.M. Mayer, S. Lee, H. Liao, B.C. Rostro, A. Fuentes, P.T. Scully, et al. *ACS Nano*, 2008,**2**,687-692.
  - 38 C.J. Orendorff, T.M. Alam, D.Y. Sasaki, B.C. Bunker, J.A. Voigt. *ACS Nano*, 2009,**3**,971-983.
  - 39 H. Takahashi, Y. Niidome, T. Niidome, K. Kaneko, H. Kawasaki, S. Yamada. *Langmuir*, 2006,**22**,2-5.
  - 40 E.T. Castellana, R.C. Gamez, D.H. Russell. *J. Am. Chem. Soc.*, 2011,**133**,4182-4185.
  - 41 B. Nikoobakht, M.A. El-Sayed. *Chem. Mater.*, 2003,**15**,1957-1962.
  - 42 E. Matijevic, W.P. Hsu. *J. Colloid Interface Sci.*, 1987,**118**,506-523.
  - 43 D.M. Yang, X.J. Kang, P.A. Ma, Y.L. Dai, Z.Y. Hou, Z.Y. Cheng, et al. *Biomaterials*, 2013,**34**,1601-1612.
  - 44 X.C. Ye, L.H. Jin, H. Caglayan, J. Chen, G.Z. Xing, C. Zheng, et al. *ACS Nano*, 2012,**6**,2804-2817.
  - 45 L.M. Liz-Marzan, M. Giersig, P. Mulvaney. *Langmuir*, 1996,**12**,4329-4335.
  - 90 Y.L. Wang, L. Cai, Y.N. Xia. *Adv. Mater.*, 2005,**17**,473-477.
  - 47 H.J. Fan, M. Knez, R. Scholz, D. Hesse, K. Nielsch, M. Zacharias, et al. *Nano Letters*, 2007,**7**,993-997.
  - 48 M.J. Kim, J.H. Park, K.Y. Lee, S. Lee, G.S. Han, H.J. Song, et al. *ACS Appl. Mater. Inter.*, 2014,**6**,1145-1151.
  - 95 W.S. Wang, M. Dahl, Y.D. Yin. *Chem. Mater.*, 2013,**25**,1179-1189.
  - 50 H. Zhang, D. Xu, Y. Huang, X.F. Duan. *Chem. Commun.*, 2011,**47**,979-981.
  - 51 G.K. Das, T.T.Y. Tan. *J. Phys. Chem. C*, 2008,**112**,11211-11217.
  - 100 J. Yang, C.M. Zhang, C. Peng, C.X. Li, L.L. Wang, R.T. Chai, et al. *Chem.-Eur. J.*, 2009,**15**,4649-4655.
  - 52 C.H. Chou, C.D. Chen, et al. *J. Phys. Chem. B*, 2005,**109**,11135-11138.
  - 53 M. Saboktakin, X.C. Ye, S.J. Oh, S.H. Hong, A.T. Fafarman, U.K. Chettiar, et al. *ACS Nano*, 2012,**6**,8758-8766.
  - 105 D.C. Drummond, M. Zignani, J.C. Leroux. *Prog. Lipid Res.*, 2000,**39**,409-460.
  - 56 W.W. Gao, J.M. Chan, O.C. Farokhzad. *Mol. Pharm.*, 2010,**7**,1913-1920.
  - 57 J.V. Jokerst, T. Lobovkina, R.N. Zare, S.S. Gambhir. *Nanomedicine*, 2011,**6**,715-728.
  - 110